*Article*

# Influence of the Elastic-Plastic Dynamic Artificial Boundary on the Progressive Collapse Performance of Truss Structures

**Jiawen Mao [1] and Jinsan Ju [1,2,*]**

1    School of Mechanics and Civil Engineering, China University of Mining & Technology—Beijing, Beijing 100083, China; BQT1900603022@student.cumtb.edu.cn
2    College of Water Resources and Civil Engineering, China Agricultural University, Beijing 100083, China
*    Correspondence: jujinsan@cau.edu.cn

**Abstract:** The traditional fixed boundary could not transmit the elastic-plastic stress waves in the progressive collapse analysis of the truss structures, leading to discrepancies in understanding the true response of structures. To solve the critical problem, a new dynamic artificial boundary is proposed and integrated into the truss structure to transmit elastic-plastic stress waves. The new dynamic artificial boundary is established through the integration of the elastic-plastic constitutive model into the governing equation of the stress wave. This boundary is subsequently implemented within the ABAQUS finite element software for the purpose of conducting progressive collapse analysis of the truss structures. The progressive collapse simulation of the truss structures involves a comparative analysis between the new dynamic artificial boundary and the traditional fixed boundary. Numerical analysis demonstrates that the dynamic artificial boundary led to varied initial failure and collapse compared to the fixed boundary. The failure typically occurs at the mid-span under the dynamic boundary. In contrast, additional failures occur near the support columns under the fixed boundary due to stress wave reflections. The dynamic artificial boundary more closely reflects the physical reality and provides a new method for the progressive collapse analysis of the truss structures in practical applications.

**Keywords:** progressive collapse; reflected waves at the boundary; dynamic artificial boundary element; truss structure

## 1. Introduction

The progressive collapse of space structures is a process of dynamic instability [1]. In this process, the impact of stress wave transmission on the elastoplastic members cannot be ignored due to the extremely short time of structural instability [2]. It is customary in the computational modeling of space structures to simplify the boundary conditions to facilitate calculation. Generally, these structures are assumed to have fixed boundaries [3]. However, the assumption of a fixed boundary is inconsistent with the actual physical situation. This assumption places a significant limitation on accurately simulating the real physical reaction of the structure when stress wave propagation is taken into account [4]. When the stress waves within a structure encounter a fixed boundary, they are reflected back into the structure [5]. The occurrence of wave reflection may lead to inaccurate predictions of stress wave effects and potential collapse mechanisms [6]. Consequently, it is worthwhile to explore this difference between simplified models and real physical conditions.

The propagation theory of elastic waves was formulated as early as the 19th century [7]. Unlike the elastic wave, the propagation theory of the plastic wave was developed relatively late [8]. When the material has non-elastic qualities, the stress-strain relationship becomes significantly more complicated, and plastic wave propagation within the member is a real possibility in such conditions. Thus, it is imperative to select a suitable constitutive model for investigating the transmission of elastic-plastic waves. Initially, constitutive

models predominantly employed linear elastic formulations predicated on Hooke's Law. These models apply to materials that have returned to their initial shape after removing stress [9]. While these models are sufficient for standard elastic materials under normal stress conditions, they were found to be inadequate when applied to elastoplastic materials [10]. Recognizing the limitations of linear models, researchers developed elastoplastic constitutive models based on Drucker-Prager, Von Mises, and Tresca criteria [11].

In recent years, with the development of materials and the improvements in measuring instruments, more elastoplastic constitutive models have been proposed. Alessandro Zona proposed an elastoplastic model following a consistent approach based on a rheological scheme leading to a simple constitutive law involving only one internal variable. The adopted formulation allows a straightforward physical interpretation and identification of the constitutive parameters of the model as well as an explicit computation of the response quantities related to failure and dissipated energy [12]. Omid Pourhosseini proposed an elastoplastic constitutive model to describe the nonlinear behavior of intact rocks under static loading [13]. Ly Xu developed an elastoplastic constitutive model to simulate the cyclic hardening and softening of the low-yield-point steel BLY160 by introducing a modified Chaboche kinematic hardening [14]. Changqing Wang presented a constitutive model of FRAC to predict the unloading path, reloading path, residual strain development, and damage evolution for the composite accounting for fiber content [15]. Changqing Wang proposed a modified constitutive model of FRAC. The effects of the fiber reinforcing factors (RI) for peak stress and critical strains were quantified and coupled into the modified [16].

To ensure that stress waves at a structural boundary propagate unimpeded from a nearby location to an infinitely distant location, the most effective method is to impose the absorbing boundary condition [17]. In recent years, various artificial boundary conditions have been applied in the field of structural engineering, such as the viscous boundary, paraxial boundary, transmitting boundary, and viscoelastic boundary. The viscous boundary mitigates the impact of stress waves by employing a sequence of dampers along the boundary to absorb their energy [18]. The paraxial boundary utilizes the paraxial approximation formula to differentiate between the waves outside and inside the computing zone, efficiently eliminating the phenomenon of reflected waves [19]. Transmitting uses multiple transmission boundaries to simulate the process of external waves passing through the boundary to achieve the propagation of waves towards infinity [20]. The viscoelastic boundary is equivalent to springs and dampers with universal physical significance [21]. However, the preceding artificial boundary conditions are mainly derived based on elastic theory, which may become ineffective or inaccurate for nonlinear materials.

The prior computational models of space structures for progressive collapse analysis often assume boundaries to fixed boundaries. This simplification fails to represent the actual physical conditions accurately. It overlooks the stress wave propagation during structural instability, which can lead to inaccurate predictions of stress wave effects and collapse mechanisms. In addition, the current dynamic boundaries are established heavily based on the constitutive model and are inadequate for elastoplastic materials where the stress-strain relationship is more complex. The present methods cannot accurately consider the propagation of elastic-plastic stress waves in the analysis of the progressive collapse of space structures, which hinders our modeling and prediction of the response of space structures. Therefore, it is necessary to develop new dynamic artificial boundaries to study the complexity of elastic-plastic wave propagation in space structures to provide a more comprehensive and accurate representation of structural responses under progressive collapse.

In this paper, an elastic-plastic dynamic artificial boundary condition suitable for numerical calculation is provided. The mathematical form of the dynamic artificial boundary equation is derived based on the elastic-plastic stress wave solution. An implementation of the elastic-plastic dynamic artificial boundary in ABAQUS is presented, utilizing the finite element method. Then, a typical numerical example for elastic-plastic stress wave propa-

gation under pulse load is selected to verify the absorption performance of the proposed dynamic artificial boundary. Finally, the progressive collapse of the truss structure under the dynamic artificial boundary condition is analyzed and compared with the result of the traditional fixed boundary condition.

The dynamic artificial boundary more closely reflects the physical reality. It provides a novel and more effective method for the progressive collapse analysis of truss structures, particularly in practical engineering applications. This alignment with real-world behavior not only enhances the accuracy of collapse predictions, but also aids in developing more robust design strategies and retrofitting techniques for truss structures, ensuring greater safety and resilience in civil engineering constructions. Dynamic modeling is crucial in regions prone to extreme events like earthquakes or blasts, where the understanding of progressive collapse mechanisms can be the difference between catastrophic failure and structural safety.

## 2. Research Significance

A new elastic-plastic dynamic artificial boundary is proposed by incorporating the elastoplastic constitutive relationship into the element equilibrium equation. The proposed elastic-plastic dynamic artificial boundary is integrated into progressive collapse analysis to mitigate the adverse effects of wave reflections on the structure. This approach is more closely related to physical reality. It enhances the realism and accuracy of collapse simulations, bridging the gap between the numerical model and practical engineering applications in structural collapse analysis. The proposed artificial boundary provides a reference for structural engineers to calculate spatial structures in response to progressive collapse scenarios.

## 3. Control Equation of the Elastic-Plastic Wave

When subjected to impact action, elastic-plastic members may display distinct regions of deformation known as the elastic zone and the plastic zone, as dictated by their motion and deformation properties. The appearance of elastic waves resulting from elastic deformation occurs earlier in comparison to plastic waves due to the comparatively high modulus of elasticity.

When the dynamic impact is applied to the structural surface, the symmetrical radial or circumferential disturbance may be induced in a cylindrical member with a uniform cross-section. The disturbance will cause the compression or torsional wave to propagate through the elastic-plastic cylindrical member. The microelement of the elastic-plastic cylindrical member is extracted for analysis, as depicted in Figure 1.
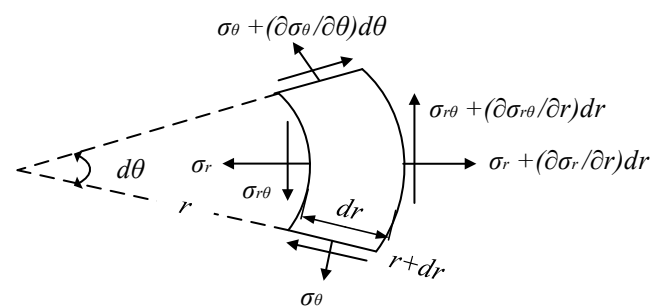


**Figure 1.** The schematic diagram of the elastic-plastic cylindrical microelement.

### 3.1. Elastic-Plastic Compression Wave

In the compression deformation mode, the stress waves propagating in the elastoplastic cylindrical member are axisymmetric compression waves. The cylindrical coordinates can be used to calculate the motion of the microelement. The variables $t$ and $r$ can represent

all state parameters due to the non-zero displacement in radial orientation. Thus, the corresponding motion equation in the radial direction can be expressed as follows.

$$\rho \frac{\partial^2 u_r}{\partial t^2} = \frac{\partial \sigma_r}{\partial r} + \frac{\sigma_r - \sigma_\theta}{r} \tag{1}$$

where $r$ and $t$ represent the radial coordinate and time coordinate, respectively, $\sigma_r$ and $\sigma_\theta$ represent radial and circumferential stress, respectively, $u_r$ represents radial displacement, and $\rho$ represents material density.

The strain components of the elastic-plastic cylindrical microelement are expressed as follows.

$$\varepsilon_r = -\frac{\partial u_r}{\partial r}, \varepsilon_\theta = -\frac{u_r}{r}, \gamma_{r\theta} = -\frac{\partial u_\theta}{\partial r} \tag{2}$$

where $\varepsilon_r$, $\gamma_{r\theta}$, and $\varepsilon_\theta$ represent the radial, shear, and circumferential strain, respectively, $u_r$ represents radial displacement, and $u_\theta$ represents circumferential displacement.

When the elastic wave reaches the position $r$ of the cylindrical member, the microelement undergoes elastic deformation. The constitutive law of material in the elastic stage can be expressed using the generalized Hooke's law.

$$\begin{bmatrix} \sigma_r \\ \sigma_\theta \\ \tau_{r\theta} \end{bmatrix} = \begin{bmatrix} K + 4G_0/3 & K - 2G_0/3 & 0 \\ K - 2G_0/3 & K + 4G_0/3 & 0 \\ 0 & 0 & G_0 \end{bmatrix} \begin{bmatrix} \varepsilon_r \\ \varepsilon_\theta \\ \gamma_{r\theta} \end{bmatrix} \tag{3}$$

where $\sigma_r$, $\sigma_\theta$, and $\tau_{r\theta}$ represent the radial, circumferential, and shear stress, respectively, $K$ represents bulk modulus, and $G_0$ represents elastic shear modulus.

The motion expression of the elastic compression wave can be obtained through the substitution of Equations (2) and (3) into Equation (1) as follows.

$$\frac{\partial^2 u_r}{\partial r^2} + \frac{\partial u_r}{r \partial r} - \frac{u_r}{r^2} = \frac{1}{c_{p,0}^2} \frac{\partial^2 u_r}{\partial t^2} \tag{4}$$

where $c_{p,0} = \sqrt{(K + 4G_0/3)/\rho}$ represents the velocity of the elastic shear wave.

If $\phi_r$ is a scalar function and $u = \partial \phi_r / \partial r$ represents the partial derivative $\partial \phi_r$ to $r$, then the above motion expression of the elastic compression wave can be expressed as follows.

$$\frac{\partial^2 \phi_r}{\partial r^2} + \frac{\partial \phi_r}{r \partial r} = \frac{1}{c_{p,0}^2} \frac{\partial^2 \phi_r}{\partial t^2} \tag{5}$$

When the plastic wave reaches the position $r$ of the cylindrical member, the microelement undergoes plastic deformation. For the plastic phase, the stress expression of $\sigma_r$, $\sigma_\theta$, and $\tau_{r\theta}$ differs from that in the elastic phase. The strain-stress relationship for the nonlinear constitutive model can be obtained by introducing the plastic shear modulus $G_1$ as follows.

$$\begin{bmatrix} \sigma_r \\ \sigma_\theta \\ \tau_{r\theta} \end{bmatrix} = \begin{bmatrix} \sigma_{r0} \\ \sigma_{\theta0} \\ \tau_{r\theta0} \end{bmatrix} + \begin{bmatrix} K + 4G_1/3 & K - 2G_1/3 & 0 \\ K - 2G_1/3 & K + 4G_1/3 & 0 \\ 0 & 0 & G_1 \end{bmatrix} \begin{bmatrix} \varepsilon_r - \varepsilon_{r0} \\ \varepsilon_\theta - \varepsilon_{\theta0} \\ \gamma_{r\theta} - \gamma_{r\theta0} \end{bmatrix} \tag{6}$$

when the maximum stress reaches the initial yield strength, $\sigma_{r0}$, $\tau_{r\theta0}$, and $\sigma_{\theta0}$ represent the radial, shear, and circumferential yield stress, respectively, and $\varepsilon_{r0}$, $\gamma_{r\theta0}$, and $\varepsilon_{\theta0}$ represent the radial, shear and circumferential yield strain, respectively.

The motion expression of the plastic compression wave can be obtained through the substitution of Equations (2) and (6) into Equation (1) as follows.

$$\frac{\partial^2 u_r}{\partial r^2} + \frac{\partial u_r}{r \partial r} - \frac{u_r}{r^2} = \frac{1}{c_{p,1}^2} \frac{\partial^2 u_r}{\partial t^2} + \frac{2(G_0 - G_1)(\varepsilon_{r0} - \varepsilon_{\theta0})}{(K + 4G_1/3)r} \tag{7}$$

If $\phi_r$ is a scalar function and $u = \partial\phi_r/\partial r$ represents the partial derivative $\partial\phi_r$ to $r$, then the above motion expression of the plastic compression wave can be expressed as follows.

$$\frac{\partial}{\partial r}\left(\frac{\partial^2\phi_r}{\partial r^2} + \frac{\partial\phi_r}{r\partial r}\right) = \frac{1}{c_{p,1}^2}\frac{\partial}{\partial r}\frac{\partial^2\phi_r}{\partial t^2} + \frac{2(G_0 - G_1)(\varepsilon_{r0} - \varepsilon_{\theta 0})}{(K + 4G_1/3)r} \tag{8}$$

where $c_{p,1} = \sqrt{(K + 4G_1/3)/\rho}$ represents the velocity of the plastic compression wave. Equation (9) can be obtained by performing integration with respect to the variable $r$ on both sides of Equation (8).

$$\frac{\partial^2\phi_r}{\partial r^2} + \frac{\partial\phi_r}{r\partial r} = \frac{1}{c_{p,1}^2}\frac{\partial^2\phi_r}{\partial t^2} + \frac{2(G_0 - G_1)(\varepsilon_{r0} - \varepsilon_{\theta 0})}{(K + 4G_1/3)}Inr + L(t) \tag{9}$$

The function $t$ does not affect other state properties because the displacement, strain, and stress are derived from the function $\psi$ with respect to $r$. Thus, $L(t) = 0$ could be substituted into Equation (9).

$$\frac{\partial^2\phi_r}{\partial r^2} + \frac{\partial\phi_r}{r\partial r} = \frac{1}{c_{p,1}^2}\frac{\partial^2\phi_r}{\partial t^2} + \frac{2(G_0 - G_1)(\varepsilon_{r0} - \varepsilon_{\theta 0})}{(K + 4G_1/3)}Inr \tag{10}$$

*3.2. Elastic-Plastic Shear Wave*

In the torsional deformation mode, the stress waves propagating in the elastoplastic cylindrical member are axisymmetric shear waves. The corresponding motion equation in the circumferential direction can be expressed as follows.

$$\rho\frac{\partial^2 u_\theta}{\partial t^2} = \frac{\partial\tau_{r\theta}}{\partial r} + \frac{2\tau_{r\theta}}{r} \tag{11}$$

where $\tau_{r\theta}$ and $u_\theta$ represent the shear stress and circumferential motion, respectively. The mathematical representation for the strain component is as follows.

$$\gamma_{r\theta} = -\frac{\partial u_\theta}{\partial r} + \frac{u_\theta}{r} \tag{12}$$

The motion expression of the elastic shear wave can be obtained through the substitution of Equations (3) and (12) into Equation (11) as follows.

$$\frac{\partial^2 u_\theta}{\partial r^2} + \frac{1}{r}\frac{\partial u_\theta}{\partial r} - \frac{u_\theta}{r^2} = \frac{1}{c_{s,0}^2}\frac{\partial^2 u_\theta}{\partial t^2} \tag{13}$$

where $c_{s,0} = \sqrt{G_0/\rho}$ represents the velocity of the elastic shear wave.

If $\phi_\theta$ is a scalar function and $u_\theta = \partial\phi_\theta/\partial r$ represents the partial derivative $\partial\phi_\theta$ to $r$, then the above motion expression of the elastic shear wave can be expressed as follows.

$$\frac{\partial^2\phi_\theta}{\partial r^2} + \frac{\partial\phi_\theta}{r\partial r} = \frac{1}{c_{s,0}^2}\frac{\partial^2\phi_\theta}{\partial t^2} \tag{14}$$

The motion expression of the plastic shear wave can be obtained through the substitution of Equations (6) and (12) into Equation (11) as follows.

$$\frac{\partial^2 u_\theta}{\partial r^2} + \frac{\partial u_\theta}{r\partial r} - \frac{u_\theta}{r^2} = \frac{1}{c_{s,1}^2}\frac{\partial^2 u_\theta}{\partial t^2} + \frac{2(G_0 - G_1)\gamma_{r\theta 0}}{G_1 r} \tag{15}$$

If $\partial\phi_\theta$ is a scalar function and $u = \partial\phi_\theta/\partial r$ represents the partial derivative $\partial\phi_\theta$ to $r$, then the above motion expression of the plastic shear wave can be expressed as follows.

$$\frac{\partial}{\partial r}\left(\frac{\partial^2\phi_\theta}{\partial r^2} + \frac{\partial\phi_\theta}{r\partial r}\right) = \frac{1}{c_{s,1}^2}\frac{\partial}{\partial r}\frac{\partial^2\phi_\theta}{\partial t^2} + \frac{2(G_0 - G_1)\gamma_{r\theta0}}{G_1 r} \tag{16}$$

where $c_{s,1} = \sqrt{G_1/\rho}$ represents the velocity of the plastic shear wave. Equation (17) can be obtained by performing integration with respect to the variable $r$ on both sides of Equation (16).

$$\frac{\partial^2\phi_\theta}{\partial r^2} + \frac{\partial\phi_\theta}{r\partial r} = \frac{1}{c_{s,1}^2}\frac{\partial^2\phi_r}{\partial t^2} + \frac{2(G_0 - G_1)\gamma_{r\theta0}}{G_1 r}Inr + L(t) \tag{17}$$

The function $t$ does not affect other state properties because the displacement, strain, and stress are derived from the function $\psi$ with respect to $r$. Thus, $L(t) = 0$ could be substituted into Equation (17).

$$\frac{\partial^2\phi_\theta}{\partial r^2} + \frac{\partial\phi_\theta}{r\partial r} = \frac{1}{c_{s,1}^2}\frac{\partial^2\phi_r}{\partial t^2} + \frac{2(G_0 - G_1)\gamma_{r\theta0}}{G_1 r}Inr \tag{18}$$

## 4. Dynamic Artificial Boundary Condition

### 4.1. The Elastic Deformation Stage

To solve the above motion expression of the elastic compression wave (5), we use the method of the separation of variables, and assume that the solution can be expressed as the product of two functions as follows.

$$\phi(r,t) = \Psi(r) \cdot T(t) \tag{19}$$

Substitute Equation (19) into the wave Equation (5) to separate variables.

$$\frac{1}{T}\frac{\partial^2 T}{\partial t^2} = \frac{c_{p,0}^2}{\Psi}\left(\frac{\partial^2\Psi}{\partial r^2} + \frac{1}{r}\frac{\partial\Psi}{\partial r}\right) = -\lambda^2 \tag{20}$$

where $-\lambda^2$ represents the separation constant. The following two equations can be obtained.

$$\frac{\partial^2 T}{\partial t^2} + \frac{c_{p,0}^2 T}{\lambda^2} = 0 \tag{21}$$

$$r^2\frac{\partial^2\Psi}{\partial r^2} + r\frac{\partial\Psi}{\partial r} + \Psi r^2\lambda^2 = 0 \tag{22}$$

The solution of Equation (21) is a combination of sine and cosine functions as follows.

$$T(t) = C_1 \cdot \sin(c_{p,0}\lambda t) + C_2 \cdot \cos(c_{p,0}\lambda t) \tag{23}$$

Equation (22) is the Bessel differential equation, and the solution is as follows.

$$\Psi(r) = C_3 \cdot J_0(\lambda r) + C_3 \cdot Y_0(\lambda r) \tag{24}$$

The general solution to the cylindrical wave equation is then a product of these two solutions.

$$\phi(r,t) = \left(C_1 \cdot \sin(c_{p,0}\lambda t) + C_2 \cdot \cos(c_{p,0}\lambda t)\right)\left(C_3 \cdot J_0(\lambda r) + C_3 \cdot Y_0(\lambda r)\right) \tag{25}$$

In practice, Bessel functions of the second kind ($Y_0(\lambda r)$) often become infinite at the origin ($r = 0$), which is usually physically unacceptable for problems involving cylindrical symmetry around the origin. Therefore, $C_3$ is often set to zero in such problems, depending on the specific boundary conditions.

The Bessel functions of $J_0(\lambda r)$, the first kind, are defined by the series expansion.

$$J_0(\lambda r) = \sum_{k=0}^{\infty} \frac{(-1)^k}{k!\Gamma(k+1)} \left( \frac{\lambda r}{2} \right)^{2k} \tag{26}$$

From the above equation, it can be seen that lacking an accurate equation for a cylindrical waveform, the approximate solution of the cylindrical compression wave can be expressed as follows when the elastic wave arrives at position $r$ of the cylindrical member.

$$\phi_r(r,t) = \frac{1}{\sqrt{r}} H\left( \frac{r}{c_{p,0}} - t \right) \tag{27}$$

where $H$ represents arbitrary functions.

The radial displacement $u_r$ can be expressed as follows.

$$u_r(r,t) = -\frac{1}{2r^{3/2}} H + \frac{1}{c_{p,0}} \frac{1}{\sqrt{r}} H' \tag{28}$$

The following equations can be obtained by seeking the second-order partial derivative of $u_r(r,t)$ and $\phi_r(r,t)$ with respect to $t$, separately.

$$\frac{\partial^2 u_r(r,t)}{\partial t^2} = \frac{\partial^2}{\partial t^2} \left( \frac{\partial \phi_r}{\partial r} \right) = -\frac{1}{2r^{3/2}} H'' + \frac{1}{c_{p,0}} \frac{1}{r^{1/2}} H''' \tag{29}$$

$$\frac{\partial^2 \phi_r}{\partial t^2} = \frac{1}{\sqrt{r}} H'' \tag{30}$$

The internal load $f_r$ of the node at the dynamic artificial boundary in the radial direction can be expressed as follows.

$$\begin{aligned} f_r &= A(K+4G_0/3)\varepsilon_r + A(K-2G_0/3)\varepsilon_\theta = A(K+4G_0/3)\left( -\frac{\partial u_r}{\partial r} - \frac{u_r}{r} \right) + 2AG_0 \frac{u_r}{r} \\ &= A(K+4G_0/3)\left( -\frac{\partial^2 \phi_r}{\partial r^2} - \frac{\partial \phi_r}{r\partial r} \right) + 2AG_0 \frac{u_r}{r} = A(K+4G_0/3)(-\frac{1}{c_{s,0}^2} \frac{\partial^2 \phi_r}{\partial t^2}) + 2AG_0 \frac{u_r}{r} \end{aligned} \tag{31}$$

By substituting Equation (30) into Equation (31), the internal load $f_r$ can be expressed as follows.

$$f_r = A(K+4G_0/3)(-\frac{1}{c_{s,0}^2} \frac{1}{\sqrt{r}} H'') + 2AG_0 \frac{u_r}{r} \tag{32}$$

The following equation can be obtained by seeking the partial derivative of $f_r$ in respect to:

$$\frac{\partial f_r}{\partial t} = \frac{2AG_0}{r} \left[ \frac{\partial u_r}{\partial t} + \frac{(K+4G_0/3)r}{2G_0} \frac{1}{c_{p,0}^2} \frac{1}{\sqrt{r}} H''' \right] \tag{33}$$

By integrating Equations (32) and (33), the following equation can be obtained.

$$f_r + \frac{2r}{c_{p,0}} \frac{\partial f_r}{\partial t} = \frac{2AG_0}{r} \left( u_r + \frac{2r}{c_{p,0}} \frac{\partial u_r}{\partial t} + \frac{r^2}{c_{p,0}^2} \frac{(K+4G_0/3)}{G_0} \frac{\partial^2 u_r}{\partial t^2} \right) \tag{34}$$

Similarly, the combined expression of shear node force $f_{r\theta}$ and the corresponding $\partial f_{r\theta}/\partial r$ can be expressed as follows.

$$f_{r\theta} + \frac{2r}{c_{s,0}} \frac{\partial f_{r\theta}}{\partial t} = \frac{2AG_0}{r} \left( u_\theta + \frac{2r}{c_{s,0}} \frac{\partial u_\theta}{\partial t} + \frac{r^2}{c_{s,0}^2} \frac{\partial^2 u_\theta}{\partial t^2} \right) \tag{35}$$

### 4.2. The Plastic Deformation Stage

The motion equation of the plastic compressional wave is a nonhomogeneous equation. According to the superposition principle, the solution of the motion Equation (10) can be represented in the following manner.

$$\phi_r = E_r + F_r \tag{36}$$

Thus, the motion expression of the plastic cylindrical compressional wave can be divided into the following two equations.

$$\frac{\partial^2 E_r}{\partial r^2} + \frac{1}{r}\frac{\partial E_r}{\partial r} - \frac{1}{c_{p,1}^2}\frac{\partial^2 E_r}{\partial t^2} = 0 \tag{37}$$

$$\frac{\partial^2 F_r}{\partial r^2} + \frac{1}{r}\frac{\partial F_r}{\partial r} - \frac{1}{c_{p,1}^2}\frac{\partial^2 F_r}{\partial t^2} = \frac{2(G_0 - G_1)(\varepsilon_{r0} - \varepsilon_{\theta 0})}{(K + 4G_1/3)} lnr \tag{38}$$

The general solution for Equation (37) can be represented in a format analogous to Equation (27), as seen below.

$$E_r = \frac{1}{\sqrt{r}}H\left(\frac{r}{c_{P,1}} - t\right) \tag{39}$$

Assume that Equation (38) has a specific solution as follows.

$$F_r = \frac{2(G_0 - G_1)(\varepsilon_{r0} - \varepsilon_{\theta 0})}{(K + 4G_1/3)}\left(\frac{r^2 lnr}{4} - \frac{r^2}{4}\right) \tag{40}$$

Subsequently, ascertain whether this solution satisfies the specified criteria.

$$\begin{aligned}\frac{\partial^2 F_r}{\partial r^2} + \frac{1}{r}\frac{\partial F_r}{\partial r} &= \frac{2(G_0 - G_1)(\varepsilon_{r0} - \varepsilon_{\theta 0})}{(K + 4G_1/3)}\left(\frac{lnr}{2} + \frac{1}{4}\right) + \frac{2(G_0 - G_1)(\varepsilon_{r0} - \varepsilon_{\theta 0})}{(K + 4G_1/3)}\frac{1}{r}\left(\frac{rlnr}{2} - \frac{r}{4}\right) \\ &= \frac{2(G_0 - G_1)(\varepsilon_{r0} - \varepsilon_{\theta 0})}{(K + 4G_1/3)}lnr\end{aligned} \tag{41}$$

Thus, the solution of the plastic compressional wave can be derived from Equations (39) and (40).

$$\phi_r = \frac{1}{\sqrt{r}}H\left(\frac{r}{c_{P,1}} - t\right) + \frac{2(G_0 - G_1)(\varepsilon_{r0} - \varepsilon_{\theta 0})}{(K + 4G_1/3)}\left(\frac{r^2 lnr}{4} - \frac{r^2}{4}\right) \tag{42}$$

The radial displacement $u_r$ can be expressed as follows.

$$u_r(r,t) = -\frac{1}{2r^{3/2}}H + \frac{1}{c_{p,0}}\frac{1}{\sqrt{r}}H' + \frac{2(G_0 - G_1)(\varepsilon_{r0} - \varepsilon_{\theta 0})}{(K + 4G_1/3)}\left(\frac{rlnr}{2} - \frac{r}{4}\right) \tag{43}$$

The following equations can be obtained by seeking the second-order partial derivative of $u_r(r,t)$ and $\phi_r(r,t)$ with respect to $t$, separately.

$$\frac{\partial^2 u_r(r,t)}{\partial t^2} = \frac{\partial^2}{\partial t^2}\left(\frac{\partial \phi_r}{\partial r}\right) = -\frac{1}{2r^{3/2}}H'' + \frac{1}{c_{p,1}}\frac{1}{r^{1/2}}H''' \tag{44}$$

$$\frac{\partial^2 \phi_r}{\partial t^2} = \frac{1}{\sqrt{r}}H'' \tag{45}$$

The internal load $f_r$ of the node at the dynamic artificial boundary in the radial direction can be expressed as follows.

$$\begin{aligned}f_r &= A\sigma_{r0} + A(K + 4G_1/3)(\varepsilon_r - \varepsilon_{r0}) + A(K - 2G_1/3)(\varepsilon_\theta - \varepsilon_{\theta 0}) \\ &= A(K + 4G_1/3)\left(-\frac{\partial u_r}{\partial r} - \frac{u_r}{r}\right) + 2AG_1\frac{u_r}{r} + A\sigma_{r0} - A(K + 4G_1/3)\varepsilon_{r0} - A(K - 2G_1/3)\varepsilon_{\theta 0} \\ &= A(K + 4G_0/3)\left(-\frac{\partial^2 \phi_r}{\partial r^2} - \frac{\partial \phi_r}{r\partial r}\right) + 2AG_1\frac{u_r}{r} + A\sigma_{r0} - A(K + 4G_1/3)\varepsilon_{r0} - A(K - 2G_1/3)\varepsilon_{\theta 0}\end{aligned} \tag{46}$$

By replacing $\frac{\partial \phi_r^2(r,t)}{\partial^2 r} + \frac{\partial \phi_r(r,t)}{r\partial r}$ with $\frac{\partial \phi_r^2(x,t)}{c_{p,1}^2 \partial^2 t}$, the equation can be obtained as follows.

$$f_r = A(K + 4G_1/3)(-\frac{1}{c_{p,1}^2}\frac{\partial^2 \phi_r}{\partial t^2}) + 2AG_1\frac{u_r}{r} + \Upsilon \tag{47}$$

where $\Upsilon = A(\sigma_{r0} - (K + 4G_1/3)\varepsilon_{r0} - (K - 2G_1/3)\varepsilon_{\theta 0})$.

By substituting Equation (45) into Equation (47), the internal load $f_r$ can be expressed as follows.

$$f_r = A(K + 4G_1/3)(-\frac{1}{c_{p,1}^2}\frac{1}{\sqrt{r}}H'') + 2AG_1\frac{u_r}{r} + \Upsilon \tag{48}$$

The following equation can be derived by seeking the partial derivative of $f_r$ with respect to $t$

$$\frac{\partial f_r}{\partial t} = \frac{2AG_1}{r}\left[\frac{\partial u_r}{\partial t} + \frac{(K + 4G_1/3)r}{2G_1}\frac{1}{c_{p,1}^2}\frac{1}{\sqrt{r}}H'''\right] \tag{49}$$

By integrating Equations (48) and (49), it is feasible to eliminate any mention of the unknown function $H(r,t)$. The subsequent equation can be derived.

$$f_r + \frac{2r}{c_{p,1}}\frac{\partial f_r}{\partial t} = \frac{2AG_1}{r}(u_r + \frac{2r}{c_{p,1}}\frac{\partial u_r}{\partial t} + \frac{r^2}{c_{p,1}^2}\frac{(K + 4G_1/3)}{G_1}\frac{\partial^2 u_r}{\partial t^2}) + \Upsilon \tag{50}$$

Similarly, the expression of node shear force $f_{r\theta}$ and the corresponding $\partial f_{r\theta}/\partial r$ can be expressed as follows.

$$f_{r\theta} + \frac{2r}{c_{s,1}}\frac{\partial f_{r\theta}}{\partial t} = \frac{2AG_1}{r}(u_\theta + \frac{2r}{c_{s,1}}\frac{\partial u_\theta}{\partial t} + \frac{r^2}{c_{s,1}^2}\frac{\partial^2 u_{r\theta}}{\partial t^2}) + A(\tau_{r\theta 0} - G_1\gamma_{r\theta 0}) \tag{51}$$

## 5. A Finite Element of the Proposed Dynamic Artificial Boundary

When subjected to sudden loading, the elastic waves and plastic waves may co-occur at the impacted end of the member. Subsequently, the elastic and plastic waves propagate through the member. Therefore, it is necessary to propose a dynamic boundary element so that the absorption of the elastic waves and plastic waves can be considered simultaneously.

For the elastic-plastic wave, the changing relationship between node force $f$, node velocity $v$, and node displacement $u$ at the dynamic artificial boundary is illustrated in Figure 2. During the stage of elastic deformation, the force, velocity, and displacement relationship of the node at the dynamic artificial boundary satisfies $f = Cv + Ku$, where constants $C = \rho c_{i,0}$ and $K = aG_0/r$, $a$ represent the constant coefficient. During the stage of plastic deformation, the force, velocity, and displacement relationship of the node at the dynamic artificial boundary satisfies $f = Cv + Ku + T$, where constants $C = \rho c_{i,1}$ and $K = bG_1/r$, $b$ represent the constant coefficient. $T$ is the additional load applied on the nodes at the dynamic artificial boundary, where $T = A(\sigma_0 - (K + 4G_1/3)\varepsilon_{r0} - (K - 2G_1/3)\varepsilon_{\theta 0})$ represents the additional load in the radial direction and $T = A(\tau_{r\theta 0} - G_1\gamma_{r\theta 0})$ represents the additional load in the circumferential direction.

The present study introduces a novel dynamic artificial boundary condition that incorporates the temporal derivative of the boundary stress. Therefore, the incorporation of the boundary condition within the finite element analysis could be achieved by numerically integrating the boundary equations over time. In this paper, the proposed dynamic artificial boundary element for elastic-plastic wave propagation is out in the ABAQUS software. This element comprises a line connecting two nodes, and the relative motion of the element node is defined by node force $f$, velocity $v$, and displacement $u$.
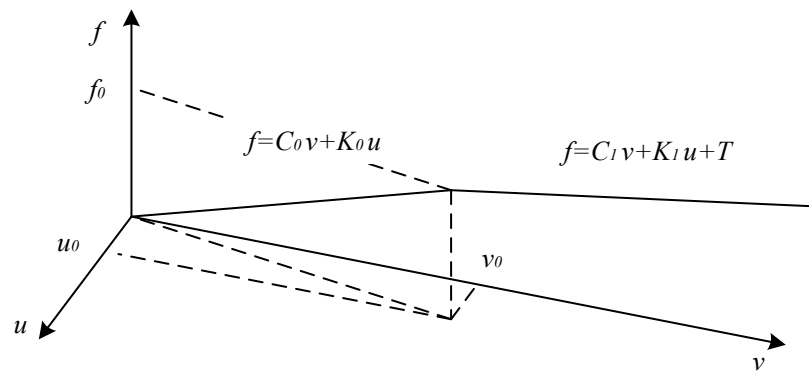
**Figure 2.** The relationship between node force $f$, velocity $v$, and displacement $u$.

The validity of the proposed dynamic artificial boundary element is examined through a numerical model of the elastic-plastic member subjected to impact. The dynamic artificial boundary elements are applied at the lower and lateral sides of the structure, and the impact load is applied at point E, as seen in Figure 3. A time history of the impact load is displayed in Figure 4. The peak load $F_{max}$ includes two situations during the loading process, and one is less than $f_0$ (yield force) to ensure that the medium does not enter plastic deformation. The other one is greater than $f_0$ to ensure that the medium would undergo plastic deformation.
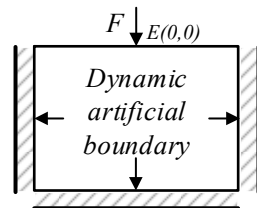


**Figure 3.** Numerical calculation model.
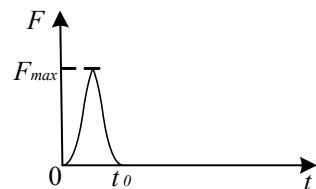


**Figure 4.** Time history of pulse load.

The size of the elastic-plastic member is 100 m $\times$ 100 m, and the material specifications of the member are concluded as Poisson's ratio = 0.3, material density = 7850 kg/m$^3$, Young's modulus = 206 $\times$ 10$^5$ MPa, and yield strength = 345 MPa.

As illustrated in Figure 5, the time history curve of the vertical displacement at point E under the dynamic artificial boundary condition is observed. The finite element calculation result of the vertical displacement under the dynamic artificial boundary condition is denoted by the solid line, and the dotted line corresponds to the exact solution of the vertical displacement. Under the dynamic artificial boundary condition, it can be observed that the calculated vertical displacement at point E shows a high level of concordance with the exact solution. During the phase of elastic deformation, the calculated vertical displacement at point E tends to zero with the increase in time, as illustrated in Figure 5a. During the phase of the plastic deformation, the calculated vertical displacement at point E tends to a non-zero value due to the residual plastic deformation, as illustrated in Figure 5b.
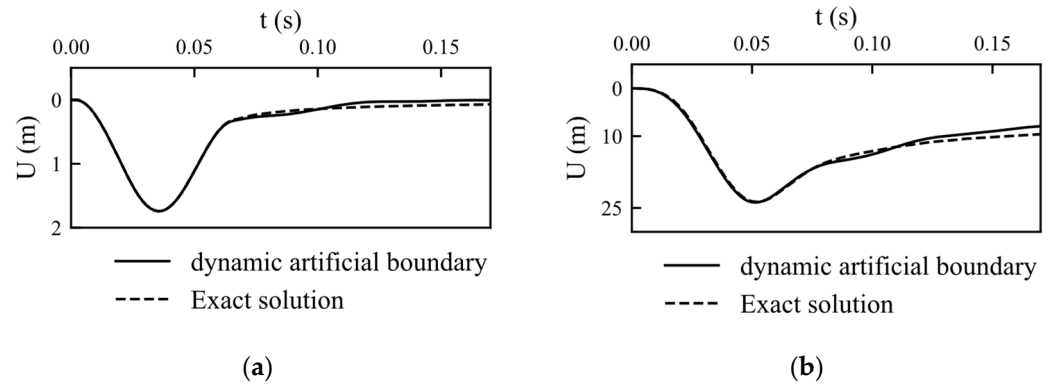
**Figure 5.** The vertical displacements of point E under the dynamic artificial boundary condition. (**a**) During the phase of elastic deformation. (**b**) During the phase of plastic deformation.

## 6. Progressive Collapse Analysis of a Truss Structure Based on the Dynamic Artificial Boundary Condition

### 6.1. The Truss Model

A truss model is constructed using the ABAQUS commercial program with a size of 30 m × 2.3 m, as shown in Figure 6. The main dimensions of the cross-section of the bars are $\varphi 186 \times 12$, $\varphi 100 \times 5$, $\varphi 86 \times 4$, and $\varphi 80 \times 3.5$.
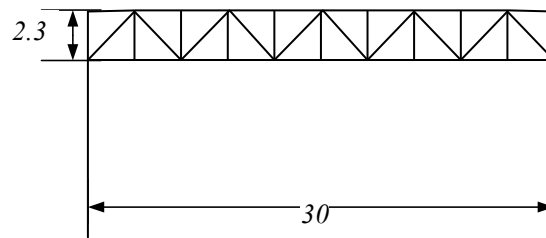


**Figure 6.** The truss model.

The truss model is constructed using Q345 steel, and the constitutive model of the Q345 uses the bilinear elastic-plastic model, as illustrated in Figure 7. The material specifications of the Q345 are concluded as elastic modulus ($E_0$) = $2 \times 10^5$ MPa, yield stress ($\sigma_0$) = 345 MPa, ultimate stress ($\sigma_1$) = 460 MPa, yield strain ($\varepsilon_0$) = $1.73 \times 10^{-3}$ mm, ultimate strain ($\varepsilon_1$) = $8 \times 10^{-3}$ mm, and Poisson's ratio = 0.3, according to CY Wan et al. [22] and F Wang et al. [23].
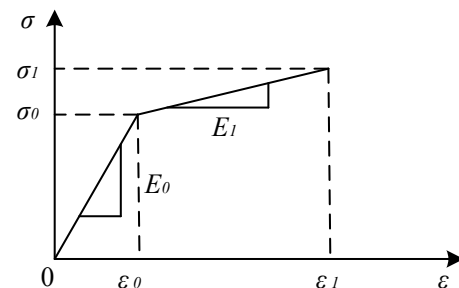


**Figure 7.** The constitutive model.

The B31 (Timoshenko beam element) is used for the simulation of all the structural members. To establish a suitable finite element size, we chose different mesh sizes for the convergence analysis. The size of the B31 finite element mesh is 0.02 m, according to the results of the convergence analysis. Rigid joints are used to connect the structural members, and the plane truss is supported by columns on the two edges. The proposed dynamic

boundary condition and fixed condition are used to connect the base of the structural column, respectively. The parameters of the dynamic artificial boundary are determined by applying the material parameters of the Q345 into the dynamic artificial boundary expression in above Section 5.

The dynamic explicit method is utilized in the progressive collapse of a truss structure, in which two stages with a total time of three seconds are defined, as illustrated in Figure 8. Within a time horizon of one second, the linear loading method is utilized to apply the gravity load with the purpose of making the structure enter a systemic equilibrium state following the structural deformation. Subsequently, a step load is introduced at one second to simulate the progressive collapse phenomenon in the truss structure when subjected to sudden loading. In the first time step, the gravity load is evenly applied to the truss structure. In the second time step, the external load is evenly applied to the all nodes of the truss structure.
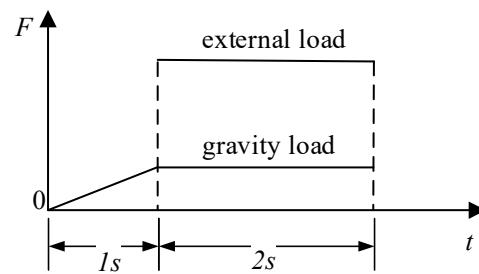


**Figure 8.** The time history of gravity and step load.

### 6.2. The Progressive Collapse Analysis

When subjected to vertical loads, the truss structure initiates a downward deformation as it begins to collapse. Consequently, it is possible to determine whether a full collapse has occurred by the observation of the node vertical displacement. While structural vertical displacement arrives at the limit state under two boundary conditions, the displacement diagram of the overall structure along the vertical direction is shown in Figure 9.
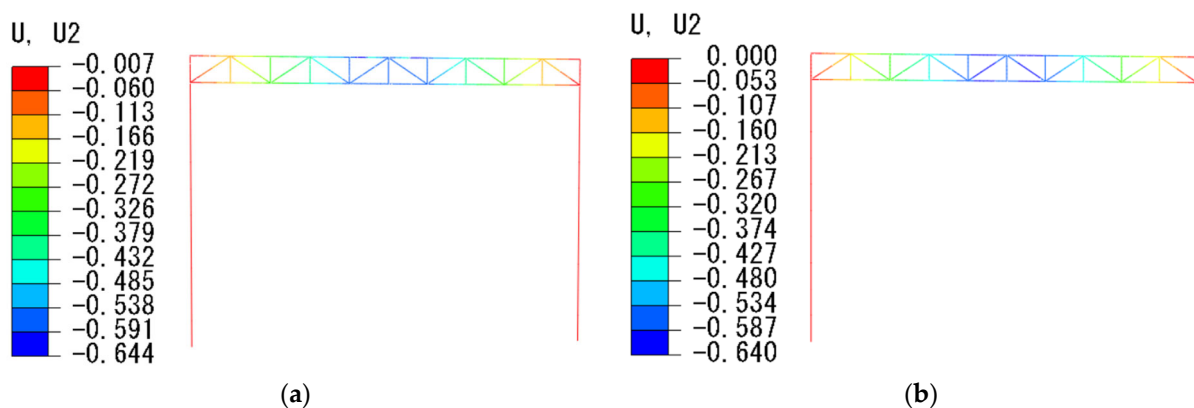


**Figure 9.** The vertical displacement diagram of the overall structure under two boundary conditions. (The unit of the vertical displacement U2 is meters (m)). (**a**) Under the dynamic artificial boundary(unit = m). (**b**) Under the fixed boundary.

The limit vertical displacement of the truss is 1/50 of the span length, with consideration of the Australian Standard AS 5100 [24]. It can be observed that the maximum vertical displacements (U2) of the structural joints both occur at the mid-span position under two boundary conditions.

The stress distribution of the members is depicted in Figure 10, considering different boundary conditions. Within 1 s, the stress of the whole structural members is lower than the plastic stress of 345 MPa, and none of the members have attained the state of plasticity.

After 1 s, when external loads are imposed on the structure, the stress of the members under the dynamic artificial boundary condition is higher than the numerical simulation results obtained with a fixed boundary. Under the dynamic artificial boundary condition, the upper chord of the truss located at the mid-span reaches a plastic state at 1.028 s, while under the fixed boundary condition, the upper chord at the mid-span enters a plastic state at 1.037 s.
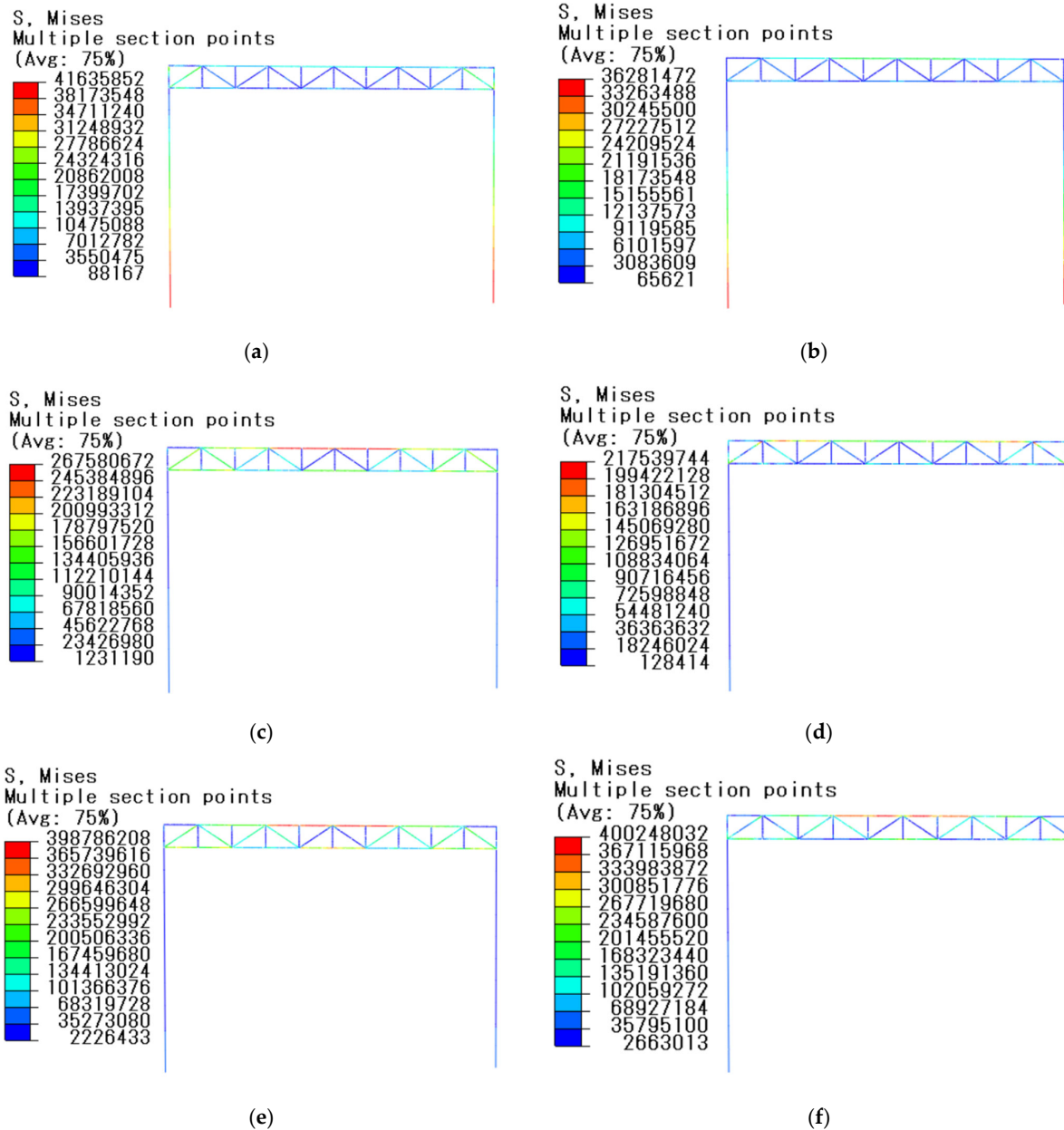
(**a**)

(**b**)

(**c**)

(**d**)

(**e**)

(**f**)

**Figure 10.** The stress distribution of the members under two boundary conditions (The stress unit is Pa). (**a**) 1 s (dynamic artificial boundary). (**b**) 1 s (fixed boundary). (**c**) 1.017 s (dynamic artificial boundary). (**d**) 1.022 s (fixed boundary). (**e**) 1.028 s (dynamic artificial boundary). (**f**) 1.037 s (fixed boundary).

The comparison between the calculation results of the vertical displacement at the mid-span under the dynamic artificial boundary condition and the fixed boundary condition is illustrated in Figure 11. The dotted line in Figure 11 represents the vertical displacement limit of structural joints at the mid-span.
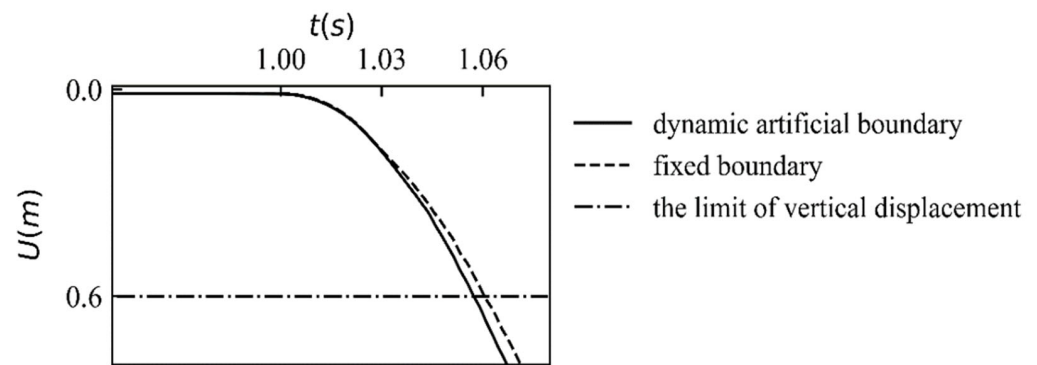
**Figure 11.** The mid-span vertical displacement of the structure over time.

The mid-span vertical displacements of the structural joints gradually increase after one second under the combined influence of the gravity load and the step load. Subsequently, the internal force is redistributed in the truss as the number of failure members increase. The rise in the internal forces sustained by the adjacent members is attributed to the redistribution of the internal loads of the failure members among the neighboring members. The process of load redistribution leads to an expansion on the extent of failure members, and a swifter decline in mid-span vertical displacement over the structure. When compared to the fixed boundary condition, the progressive collapse of the truss occurs earlier under the dynamic boundary condition in the analytical process.

The observed variations in the structural collapse mechanism are attributed to implementing different boundary conditions during the dynamic analysis.

In order to better understand the distinction between structural progressive collapse processes under different boundary conditions, the distributions of failure members are intercepted at the time point where the number of failure members grows, as illustrated in Figure 12. The curved lines represent the position of the failure members in Figure 12.
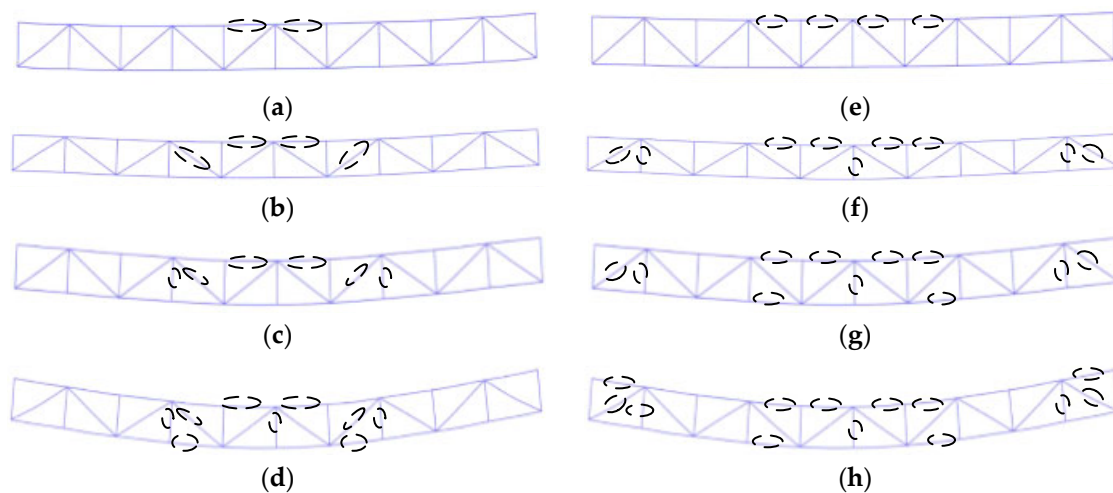


**Figure 12.** The plane truss model. (**a**) 1.030 s (dynamic artificial boundary). (**b**) 1.041 s (dynamic artificial boundary). (**c**) 1.050 s (dynamic artificial boundary). (**d**) 1.058 s (dynamic artificial boundary). (**e**) 1.040 s (fixed boundary). (**f**) 1.053 s (fixed boundary). (**g**) 1.062 s (fixed boundary). (**h**) 1.066 s (fixed boundary).

For the dynamic artificial boundary condition, the upper compression members at the mid-span are the initial failure members with an occurrence time of 1.03 s. Then, the adjacent diagonal web members turn into failure, resulting in an additional escalation in the quantity of failure members. Thereafter, the vertical web members at the mid-span and the lower tension members near the mid-span also turn into failure. The region of

failure members is primarily located at the mid-span of the plane truss structure, and no failure members appear at both sides of the truss structure. During the analysis process, the high-sensitivity upper compression members first turn into failure when subjected to the upper load. Subsequently, the failure of other compression members and tensile members also occurs due to structural deformation and the redistribution of internal forces. The majority of the failure members are compression members.

For the fixed boundary condition, the emergence time of initial failure for the structural member is 1.04 s. Specifically, the failure manifests initially in the upper compression members located at the mid-span. The failure of the upper members near the mid-span occurs subsequently in a short time. Next, the failure gradually expands to web members at mid-span. Meanwhile, owing to the stress wave reflection at the fixed boundary, a substantial strain develops in the web members near the support columns with the unstable internal stress. This strain ultimately leads to the failure of the members near the support columns. Finally, the failure region occurs at the lower members near the mid-span and the upper members near the support. For the fixed boundary condition, it is noteworthy that failure members would appear near the support columns on both sides, except the middle of the structure.

When the dynamic boundary condition is applied, it is possible to draw the conclusion that the progressive collapse process observed in the truss structure is more realistic. If the effect of stress wave transmission at the boundary is disregarded, then the estimation of the structure's resistance to progressive collapse becomes imprecise.

## 7. Conclusions

The work aims to investigate the impact of wave reflection at the boundary on the progressive collapse resistance of a truss structure. The primary conclusions can be summarized as follows:

(1) The motion expression of the elastic-plastic stress waves is obtained through the integration of the elastoplastic constitutive model into the governing equation of the stress wave. The analytical solution for the elastic wave is obtained based on an approximate expression of the cylindrical wave, and the analytical solution for the plastic wave is obtained by applying the superposition principle.

(2) A new elastic-plastic dynamic artificial boundary condition is provided and the corresponding finite element is achieved in the truss structure analysis. The validity of the dynamic artificial boundary element is examined through a plane numerical model subjected to impact load. Based on the obtained numerical results, the provided dynamic boundary element is capable of absorbing both elastic waves and plastic waves.

(3) Under the dynamic artificial boundary condition, the failure members appear in the mid-span of the truss structure, contrasting with failure members near the support columns under fixed conditions, which means that the reflection of stress waves has a notable influence on the structural stability.

(4) Under the dynamic artificial boundary condition, the initial failure member and the subsequent structural collapse occur at an varied time, as compared to the case of the fixed boundary condition. This indicates that boundary conditions can affect the structural stability, and reasonable boundary conditions need to be used in the analysis.

**Author Contributions:** Conceptualization, methodology, analysis, and writing—original draft preparation, J.M.; writing—review and editing, supervision, J.J. All authors have read and agreed to the published version of the manuscript.

**Data Availability Statement:** Data are contained within the article.

# References

1. Suwondo, R.; Cunningham, L.; Gillie, M.; Bailey, C. Progressive collapse analysis of composite steel frames subject to fire following earthquake. *Fire Saf. J.* **2019**, *103*, 49–58. [CrossRef]
2. Rodríguez, D.; Brunesi, E.; Nascimbene, R. Fragility and sensitivity analysis of steel frames with bolted-angle connections under progressive collapse. *Eng. Struct.* **2021**, *228*, 111508. [CrossRef]
3. Corley, W.G. Lessons learned on improving resistance of buildings to terrorist attacks. *J. Perform. Constr. Facil.* **2004**, *18*, 68–78. [CrossRef]
4. Cohen, T.; Masri, R.; Durban, D. Shock waves in dynamic cavity expansion. *J. Appl. Mech.* **2010**, *77*, 041009. [CrossRef]
5. Bedford, A.; Drumheller, D.S. *Introduction to Elastic Wave Propagation*; Springer Nature: London, UK, 2023.
6. Rapoport, L.; Katzir, Z.; Rubin, M.B. Termination of the starting pmemberlem of dynamic expansion of a spherical cavity in an infinite elastic-perfectly-plastic medium. *Wave Motion* **2011**, *48*, 441–452. [CrossRef]
7. Patrick, J. Numerical methods for elastic wave propagation. In *Waves in Nonlinear Pre-Stressed Materials*; Springer: Vienna, Austria, 2007; pp. 181–281.
8. Wang, Z.G.; Meyer, L.W. On the plastic wave propagation along the specimen length in SHPB test. *Exp. Mech.* **2010**, *50*, 1061–1074. [CrossRef]
9. Brown, L.B.; Dorman, S.G.; Burns, J.T. Incorporation of high-altitude environmental effects in the linear elastic fracture mechanics-based modeling of aluminum alloy 7075. *Fatigue Fract. Eng. Mater. Struct.* **2022**, *45*, 2516–2530. [CrossRef]
10. Sadeghian, F.; Haddad, A.; Jahandari, S.; Rasekh, H.; Ozbakkaloglu, T. Effects of electrokinetic phenomena on the load-bearing capacity of different steel and concrete piles: A small-scale experimental study. *Can. Geotech. J.* **2021**, *58*, 741–746. [CrossRef]
11. Giraldo-Londoño, O.; Paulino, G.H. A unified approach for topology optimization with local stress constraints considering various failure criteria: Von Mises, Drucker–Prager, Tresca, Mohr–Coulomb, Bresler–Pister and Willam–Warnke. *Proc. R. Soc. A* **2020**, *476*, 20190861. [CrossRef]
12. Zona, A.; Andrea Dall'Asta, A. Elastoplastic model for steel buckling-restrained braces. *J. Constr. Steel Res.* **2012**, *68*, 118–125. [CrossRef]
13. Pourhosseini, O.; Shabanimashcool, M. Development of an elasto-plastic constitutive model for intact rocks. *Int. J. Rock Mech. Min. Sci.* **2014**, *66*, 1–12. [CrossRef]
14. Xu, L.Y.; Fan, J.S.; Yang, Y.; Tao, M.X.; Tang, Z.Y. An improved elasto-plastic constitutive model for the exquisite description of stress-strain hysteresis loops with cyclic hardening and softening effects. *Mech. Mater.* **2020**, *150*, 103590. [CrossRef]
15. Wang, C.; Xiao, J.; Liu, W.; Ma, Z. Unloading and reloading stress-strain relationship of recycled aggregate concrete reinforced with steel/polypropylene fibers under uniaxial low-cycle loadings. *Cem. Concr. Compos.* **2022**, *131*, 104597. [CrossRef]
16. Wang, C.; Wu, H.; Li, C. Hysteresis and damping properties of steel and polypropylene fiber reinforced recycled aggregate concrete under uniaxial low-cycle loadings. *Constr. Build. Mater.* **2022**, *319*, 126191. [CrossRef]
17. Peng, L.; Song, E.-X. A high-order time-domain transmitting boundary for cylindrical wave propagation pmemberlems in unbounded saturated poroelastic media. *Soil Dyn. Earthq. Eng.* **2013**, *48*, 48–62.
18. Xin, B.; Liu, J.-B.; Li, S.-T.; Wang, F. A new viscoelastic artificial boundary with improved numerical stability in explicit calculation of wave propagation pmemberlems in infinite domains. *Comput. Geotech.* **2022**, *145*, 104698. [CrossRef]
19. Zhang, W.; Lim, K.; Ghahari, S.F.; Arduino, P.; Taciroglu, E. On the implementation and validation of a three-dimensional pressure-dependent bounding surface plasticity model for soil nonlinear wave propagation and soil-structure interaction analyses. *Int. J. Numer. Anal. Methods Geomech.* **2021**, *45*, 1091–1119. [CrossRef]
20. Wang, F.; Song, Z.; Liu, Y.; Luo, B. Seismic wave input method for high earth dams considering the transmission amplification effect of the bedrock–overburden interface. *Comput. Geotech.* **2021**, *130*, 103927. [CrossRef]
21. Patil, R.; Joladarashi, S.; Kadoli, R. Bending and vibration studies of FG porous sandwich beam with viscoelastic boundary conditions: FE approach. *Mech. Adv. Mater. Struct.* **2023**, *30*, 3588–3607. [CrossRef]
22. Wan, C.Y.; Zha, X.X. Nonlinear analysis and design of concrete-filled dual steel tubular columns under axial loading. *Steel Compos. Struct.* **2016**, *20*, 571–597. [CrossRef]
23. Wang, F.; Su, M.; Hong, M.; Guo, Y.; Li, S. Cyclic behaviour of Y-shaped eccentrically braced frames fabricated with high-strength steel composite. *J. Constr. Steel Res.* **2016**, *120*, 176–187. [CrossRef]
24. Nicholas, A. The new Australian Standard AS 5100-part 9: Timber bridges. In Proceedings of the 9th Austroads Bridge Conference, Sydney, New South Wales, Australia, 22–24 October 2014.